

# 1 Development and External Validation of a 2 Mixed-Effects Deep Learning Model to 3 Diagnose COVID-19 from CT Imaging

4 Joshua Bridge, Yanda Meng, Wenyue Zhu, Thomas Fitzmaurice, Caroline McCann, Cliff Addison,  
5 Manhui Wang, Cristin Merritt, Stu Franks, Maria Mackey, Steve Messenger, Renrong Sun, Yitian  
6 Zhao, Yalin Zheng

7 Institute of Life Course and Medical Sciences, University of Liverpool, Liverpool, United Kingdom, L7  
8 8TX Joshua Bridge PhD. Student, Yanda Meng PhD. Student, Wenyue Zhu PhD. Student, Thomas  
9 Fitzmaurice Clinical Research Fellow in Respiratory Medicine, Yalin Zheng Reader in Ophthalmic  
10 Imaging. Department of Respiratory Medicine, Liverpool Heart and Chest Hospital NHS Foundation  
11 Trust, Liverpool, United Kingdom, L14 3PE Thomas Fitzmaurice Clinical Research Fellow in  
12 Respiratory Medicine. Department of Radiology, Liverpool Heart and Chest Hospital NHS Foundation  
13 Trust, United Kingdom, L14 3PE Caroline McCann Consultant Cardiothoracic Radiologist. Advanced  
14 Research Computing, University of Liverpool, Liverpool, United Kingdom, L69 3BX Cliff Addison,  
15 Manhui Wang. Alces Flight Limited, Bicester, United Kingdom, OX26 4PP Cristin Merritt, Stu Franks.  
16 Amazon Web Services, 60 Holborn Viaduct, London EC1A 2FD Maria Mackey, Steve Messenger.  
17 Department of Radiology, Hubei Provincial Hospital of Integrated Chinese and Western Medicine,  
18 Hubei University of Chinese Medicine, Wuhan 430000, China Renrong Sun. Cixi Institute of  
19 Biomedical Engineering, Ningbo Institute of Materials Technology and Engineering, Chinese  
20 Academy of Sciences, Ningbo 315201, China Yitian Zhao.

21  
22 Correspondence to:

23 Dr Yalin Zheng,  
24 Institute of Life Course and Medical Sciences,  
25 University of Liverpool,  
26 William Henry Duncan Building,  
27 6 West Derby Street,  
28 Liverpool,  
29 L7 8TX,  
30 [Yalin.Zheng@liverpool.ac.uk](mailto:Yalin.Zheng@liverpool.ac.uk)  
31

## 1 Abstract

### 2 Objectives

3 To develop and externally geographically validate a mixed-effects deep learning model to diagnose  
4 COVID-19 from computed tomography (CT) imaging following best practice guidelines and assess the  
5 strengths and weaknesses of deep learning COVID-19 diagnosis.

### 6 Design

7 Model development and external validation with retrospectively collected data from two countries.

### 8 Setting

9 Hospitals in Moscow, Russia, collected between March 1, 2020, and April 25, 2020. The China  
10 Consortium of Chest CT Image Investigation (CC-CCII) collected between January 25, 2020, and  
11 March 27, 2020.

### 12 Participants

13 1,110 and 796 patients with either COVID-19 or healthy CT volumes from Moscow, Russia, and  
14 China, respectively.

### 15 Main outcome measures

16 We developed a deep learning model with a novel mixed-effects layer to model the relationship  
17 between slices in CT imaging. The model was trained on a dataset from hospitals in Moscow, Russia,  
18 and externally geographically validated on a dataset from a consortium of Chinese hospitals. Model  
19 performance was evaluated in discriminative performance using the area under the receiver  
20 operating characteristic (AUROC), sensitivity, specificity, positive predictive value (PPV), and negative  
21 predictive value (NPV). In addition, calibration performance was assessed using calibration curves,  
22 and clinical benefit was assessed using decision curve analysis. Finally, the model's decisions were  
23 assessed visually using saliency maps.

### 24 Results

25 External validation on the large Chinese dataset showed excellent performance with an AUROC of  
26 0.936 (95%CI: 0.910, 0.961). Using a probability threshold of 0.5, the sensitivity, specificity, NPV, and  
27 PPV were 0.753 (0.647, 0.840), 0.909 (0.869, 0.940), 0.711 (0.606, 0.802), and 0.925 (0.888, 0.953),  
28 respectively.

### 29 Conclusions

30 Deep learning can reduce stress on healthcare systems by automatically screening CT imaging for  
31 COVID-19. However, deep learning models must be robustly assessed using various performance  
32 measures and externally validated in each setting. In addition, best practice guidelines for  
33 developing and reporting predictive models are vital for the safe adoption of such models.

34

## 1 Statements

2 The authors do not own any of the patient data, and ethics approval was not needed. The lead  
3 author affirms that this manuscript is an honest, accurate, and transparent account of the study  
4 being reported, that no important aspects of the study have been omitted, and that any  
5 discrepancies from the study as planned (and, if relevant, registered) have been explained. Patients  
6 and the public were not involved in the study.

## 7 Funding

8 This study was funded by EPSRC studentship (No. 2110275), EPSRC Impact Acceleration Account  
9 (IAA) funding, and Amazon Web Services.

## 10 Summary

11 What is already known on this topic

- 12 • Deep learning can diagnose diseases from imaging data automatically
- 13 • Many studies using deep learning are of poor quality and fail to follow current best practice  
14 guidelines for the development and reporting of predictive models
- 15 • Current methods do not adequately model the relationship between slices in CT volumetric  
16 data

17 What this study adds

- 18 • A novel method to analyse volumetric imaging data composed of slices such as CT images  
19 using deep learning
- 20 • Model developed following current best-practice guidelines for the development and  
21 reporting of prediction models

22

## 1 Introduction

2 Coronavirus disease 2019 (COVID-19) is an infectious respiratory disease caused by severe acute  
3 respiratory syndrome coronavirus 2 (SARS-CoV-2). Virus clinical presentation ranges from mild cold-  
4 like symptoms to severe viral pneumonia, which can be fatal.<sup>1</sup> While some countries have achieved  
5 relative control through lockdowns, future outbreaks and new strains are expected to continue, with  
6 many experts believing the virus is here to stay.<sup>2</sup> Detection and isolation is the most effective way to  
7 prevent further spread of the virus. Even with effective vaccines becoming widely available, with the  
8 threat of continued waves and new potentially vaccine-resistant variants, it is vital to further  
9 develop diagnostic tools for COVID-19. These tools will likely also apply to future outbreaks of other  
10 similar diseases as well as common diseases such as pneumonia.

11 The diagnosis of COVID-19 is usually determined by Reverse Transcription Polymerase Chain  
12 Reaction (RT-PCR), but this is far from being a gold standard. A negative test does not necessarily  
13 indicate a negative diagnosis, with one recent review finding that RT-PCR has a real-world sensitivity  
14 of around 70% and a specificity of 95%.<sup>3</sup> Furthermore, an individual patient data systematic review<sup>4</sup>  
15 found that RT-PCR often fails to detect COVID-19, and early sampling is key to reducing false  
16 negatives. Therefore, these tests are often more helpful to rule in COVID-19 rather than ruling out.  
17 If a patient presents with symptoms of COVID-19, but an RT-PCR test is negative, then further tests  
18 are often required.<sup>1</sup> Consecutive negative tests with at least a one-day gap are recommended;  
19 however, this still does not guarantee that the patient is negative for COVID-19.<sup>5</sup> Computed  
20 tomography (CT) can play a significant role in diagnosing COVID-19.<sup>6</sup> Given the excessive number of  
21 COVID-19 cases worldwide and the strain on resources expected, automated diagnosis might reduce  
22 the burden on reporting radiologists.

23 CT images are made up of many slices, creating a three dimensional (3D)-like structure. Previous  
24 approaches, such as those used by Li et al.<sup>7</sup> and Bai et al.,<sup>8</sup> treat the image as separate slices and use  
25 a pooling layer to concatenate the slices. An alternative approach assumes the slices form a 3D  
26 structure and use a 3D CNN, such as that proposed in CoviNet.<sup>9</sup> A fundamental limitation of these  
27 methods is the need for the same number of slices as their inputs, but the number of slices often  
28 varies between different CT volumes. Instead, we propose using a novel mixed-effects layer to  
29 consider the relationship between slices in each scan. Mixed-effects models are commonly used in  
30 traditional statistics,<sup>10,11</sup> but we believe this is the first time that mixed-effects models have been  
31 utilised in such a way. It has been observed that some lobes of the lung are more often affected by  
32 COVID-19 than others<sup>12,13</sup> with lower lobe distribution being a prominent feature of COVID-19,<sup>14</sup> the  
33 fixed-effects take this into account by considering where each slice is located within the scan.

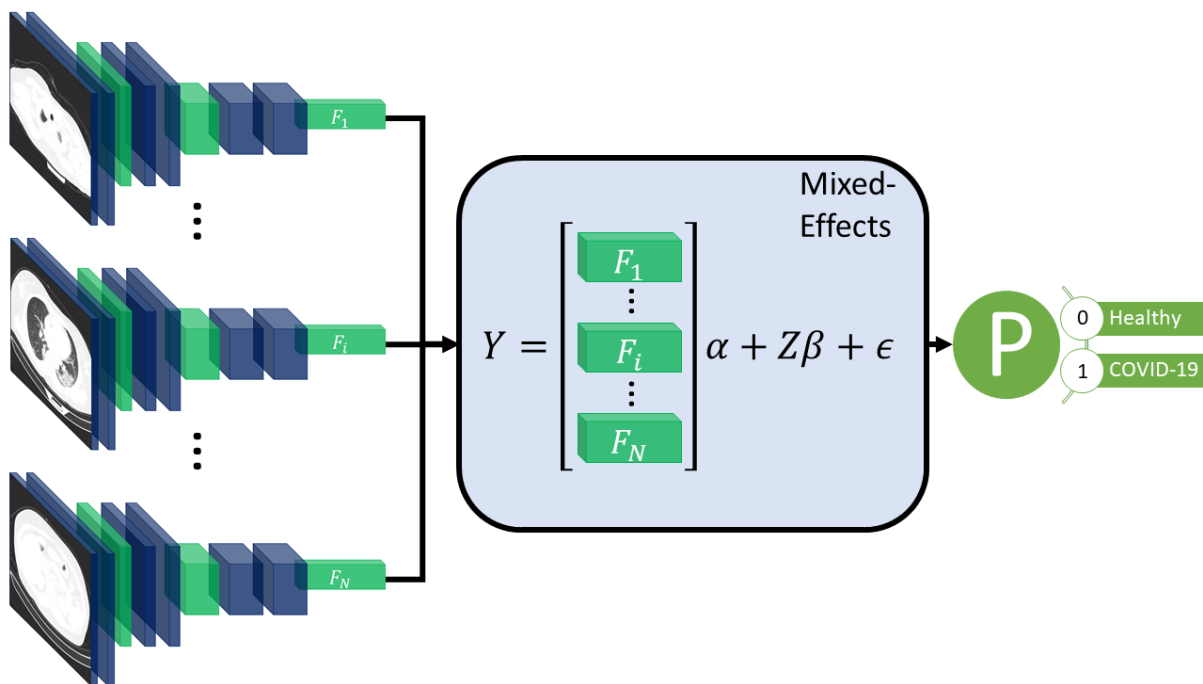
34 Deep learning has shown great potential in the automatic classification of disease, often achieving  
35 expert-level performance. Such models could screen and monitor COVID-19 by automatically  
36 analysing routinely collected CT images. As observed by Wynants et al.<sup>15</sup> and Roberts et al.,<sup>16</sup> many  
37 models are already developed to diagnose COVID-19, which often obtain excellent discriminative  
38 performance; however, very few of these models, if any, are suitable for clinical use, mainly due to a  
39 lack of robust analysis and reporting. These models often suffer from common pitfalls, making them  
40 unsuitable for broader adoption. Roberts et al.<sup>16</sup> identified three common areas in which models  
41 often fail these are: (1) a lack of adequately documented methods for reproducibility, (2) failure to  
42 follow established guidelines and best practices for the development of deep learning models, and  
43 (3) an absence of external validation displaying the model's applicability to a broader range of data  
44 outside of the study sample. Failure to address these pitfalls leads to profoundly flawed and biased  
45 models, making them unsuitable for deployment.

1 In this work, we aim to address the problems associated with previous models by following  
2 guidelines for the reporting<sup>17,18</sup> and development<sup>19</sup> of prediction models to ensure that we have  
3 rigorous documentation allowing the methods developed here to be replicated. In addition, we will  
4 make code and the trained model publicly available at [github.com/JTBridge/ME-COVID19] to  
5 promote reproducible research and facilitate adoption. Finally, we use a second dataset from a  
6 country other than the development dataset to externally validate the model and report a range of  
7 performance measures evaluating the model's discrimination, calibration, and clinical usefulness.

8 Hence, our main aim is to develop a mixed-effects deep learning model to accurately classify images  
9 as healthy or COVID-19, following best practice guidelines. Our secondary aim is to show how deep  
10 learning predictive algorithms can satisfy current best practice guidelines to create reproducible and  
11 less biased models.

## 12 Methods

13 Our proposed method consists of a feature extractor and a two-stage generalised linear mixed-  
14 effects model (GLMM),<sup>20</sup> with all parameters estimated within the deep learning framework using  
15 backpropagation. First, a series of CT slices forming a CT volume is input to the model. In our work,  
16 we use 20 slices. Next, a convolutional neural network (CNN) extract relevant features from the  
17 model and creates a feature vector for each CT slice. Then, a mixed-effects layer concatenates the  
18 feature vectors into a single vector. Finally, a fully connected layer followed by a sigmoid activation  
19 gives a probability of COVID-19 for the whole volume. The mixed effects and fully connected layer  
20 with sigmoid activation are analogous to a linear GLMM in traditional statistics. The overall  
21 framework is shown in Figure 1.



22  
23 **Figure 1: Diagram of the overall framework.** Twenty slices are chosen from a CT volume. Each slice is  
24 fed into a CNN with shared weights, which outputs a feature vector of length 2048 for each image.  
25 The feature vectors form a 20-by-2048 fixed effects matrix, X, for the GMM model with a random-  
26 effects matrix, Z, consisting of an identity matrix. A mixed-effects model is used to model the  
27 relationship between slices. Finally, a fully connected layer and sigmoid activation return a  
28 probability of the diagnosis.

## 1 Feature extractor

2 For the feature extractor, we use a CNN. In this work, we chose InceptionV3<sup>21</sup> as it is relatively  
3 efficient and commonly used. InceptionV3 outputs a feature vector of length 2048. To reduce the  
4 time needed to reach convergence, we pretrained the CNN on ImageNet.<sup>22</sup> A CNN is used for each  
5 slice, with shared weights between CNNs; this reduces the amount of computational power  
6 required. Following the CNN, we used a global average pooling layer to reduce each image to a  
7 feature vector for each slice. We then added a dropout of 0.6 to improve generalizability to unseen  
8 images. We form the feature vectors into a matrix of shape  $20 \times 2048$ . Although we used  
9 InceptionV3<sup>21</sup> here, other networks would also work and may provide better performance on other  
10 similar tasks. We then need to concatenate these feature vectors into a single feature vector for the  
11 whole volume; normally, pooling is used, in our work we propose using a mixed-effects models.

## 12 Mixed-effects network

13 We propose utilising a novel mixed-effects layer to model the relationship between slices. Mixed-  
14 effects models are a statistical model consisting of a fixed-effects part and a random-effects part.  
15 The fixed-effects part models the relationship within the CT slice; the random effects can model the  
16 spatial correlation between CT slices within the same image.<sup>11</sup> For volumetric data, the number of  
17 slices may differ significantly due to various factors such as imaging protocol and the size of the  
18 patient. Some volumes may have fewer images than the model is designed to use, which leads to  
19 missing data. Mixed-effects models can deal with missing data provided the data are missing at  
20 random. The mixed-effects model is given by

$$21 \quad Y_i = X_i\alpha + Z_i\beta + e_i$$

22 where  $Y_i$ ,  $X_i$ ,  $Z_i$ ,  $e_i$  are vectors of outcomes, fixed effects design matrix of shape  $20 \times 2048$ ,  
23 random effects design matrix of shape  $20 \times 20$ , and vector of error unknown random errors of the  
24  $i$ th patient of shape 20, respectively, and  $\alpha$ ,  $\beta$  are fixed and random effects parameters, both of  
25 length 20. We assume that the random effects  $\beta$  are normally distributed with 0 and variance  $G$

$$26 \quad \beta \sim N(0, G)$$

27 We also assume independence between the random effects and the error term.

28 The fixed effects design matrix,  $X$ , is made up of the feature vectors output from the feature  
29 extraction network. For the random effects design matrix,  $Z$ , we use an identity matrix with the  
30 same size as the number of slices; in our experiments, this is 20. The design matrix is then given by

$$31 \quad Z_{20 \times 20} = \begin{bmatrix} 1 & 0 & \dots & 0 & 0 \\ 0 & 1 & \dots & 0 & 0 \\ \vdots & \vdots & \ddots & \vdots & \vdots \\ 0 & 0 & \dots & 1 & 0 \\ 0 & 0 & \dots & 0 & 1 \end{bmatrix}.$$

32 This matrix easily generalises to any number of slices. If the distance between slices is not uniform,  
33 the values can be altered accordingly. We assumed no particular correlation matrix. We included the  
34 fixed and random intercept in the model. All parameters for the mixed-effects layer were initialised  
35 using the Gaussian distribution with mean 0 and standard deviation 0.05.

36 A type of mixed-effects modelling has previously been combined with deep learning for gaze  
37 estimation.<sup>23</sup> However, their mixed-effects method is very different from our proposed method;  
38 they used the same design matrix for fixed and random effects. In addition, they also estimated  
39 random-effects parameters with an expectation-maximisation algorithm, which was separate from  
40 the fixed effects estimation, which used deep learning. In our work, we utilise a spatial design matrix

1 to model the spatial relationship between slices and estimate parameters within the deep learning  
2 framework using backpropagation without the need for multiple stages.

3 Loss function

4 As the parameters in the model are all estimated using backpropagation, we must ensure that the  
5 assumption of normally distributed random effects parameters with mean zero is valid. We achieve  
6 this by introducing a loss function for the random effects parameters, which enforces a mean,  
7 skewness, and excess kurtosis of 0. We measure skewness using the adjusted Fisher–Pearson  
8 standardised moment coefficient

$$9 \quad Skew(\beta) = \frac{\sqrt{n(n-1)}}{n-2} \frac{E[(\beta - \bar{\beta})^3]}{(E[(\beta - \bar{\beta})^2])^{3/2}}$$

10 and the excess kurtosis using

$$11 \quad Kurt(\beta) - 3 = \frac{1}{n^2} \sum_{i=1}^n \left( \frac{E[(\beta - \bar{\beta})^4]}{(E[(\beta - \bar{\beta})^2])^2} - 3 \right),$$

12 where  $n$  is the length of  $\beta$ ,  $\bar{\beta}$  is the mean of  $\beta$  and  $E[\cdot]$  is the expectation function. The Gaussian  
13 distribution has a kurtosis of 3; therefore, the excess kurtosis is given by the kurtosis minus 3. This  
14 formula for this fixed-effects parameters loss function which we aim to minimise, is then given by

$$15 \quad L_{fixed} = |E(\beta) + Skew(\beta) + Kurt(\beta) - 3|.$$

16 For the classification, we use the Brier Score<sup>24</sup> as the loss function, which is given by

$$17 \quad L_{Brier} = \frac{1}{N} \sum_{i=1}^N (p_i - o_i)^2$$

18 where  $N$  is the total number of samples,  $p_i$  is the predicted probability of sample  $i$  and  $o_i$  is the  
19 observed outcome of sample  $i$ . The Brier score is the same as the mean squared error of the  
20 predicted probability.

21 We chose to use the Brier Score over the more commonly used binary cross-entropy because it can  
22 be decomposed into two components: refinement and calibration. Calibration is often overlooked in  
23 deep learning models but is vital to assess the safety of any prediction model. The refinement  
24 component combines the model's resolution and uncertainty and measures the model's  
25 discrimination. The calibration component can be used as a measure of the model calibration.  
26 Therefore, the Brier Score can be used to optimize both the discrimination and calibration of the  
27 model. The overall loss function is given by

$$28 \quad L = L_{Brier} + L_{fixed}.$$

29 A scaling factor could be introduced to weight one part of the loss function as more important than  
30 the other; however, we give both parts of the loss function equal weighting in our work.

31 We also transformed the labels as suggested by Platt<sup>25</sup> to reduce overfitting. The negative and  
32 positive labels become

$$33 \quad o_- = \frac{1}{N_- + 2}$$



1 and

$$2 \quad o_+ = \frac{N_+ + 1}{N_+ + 2}$$

3 respectively, where  $N_-$  and  $N_+$  are the total number of negative and positive cases in the training  
4 set. This is similar to label smoothing as commonly used in deep learning, but the new targets are  
5 chosen by applying Baye's Rule to the out-of-sample data to prevent overfitting.

6 Classification layer

7 The output of the mixed-effects layer is a single vector, which is the same length as the number of  
8 slices used. For example, in our work, we had a vector of length 20. Furthermore, we used a fully  
9 connected layer with sigmoid activation to obtain a probability of the scan showing COVID-19; the  
10 sigmoid activation is analogous to the logistic link function in traditional statistics. Finally, we added  
11 an L1 regularisation term of 0.1 and an L2 regularisation term of 0.01 to the kernel to reduce  
12 overfitting.

13 Model performance

14 Many deep learning models focus on assessing discriminative performance only, using measures  
15 such as the area under the receiver operating characteristic curve (AUROC), sensitivity, and  
16 specificity. To better understand the model performance and impact, we report performance  
17 measures in three broad areas: discrimination, calibration, and clinical usefulness.<sup>26</sup> Discrimination  
18 assesses how well a model can discriminate between healthy and COVID-19 positive patients.  
19 Models with excellent discriminative performance can still produce unreliable results, with vastly  
20 overestimated probabilities regardless of the true diagnosis.<sup>27</sup> Model calibration is often overlooked  
21 and rarely reported in deep learning, if at all; however, poorly calibrated models can be misleading  
22 and lead to dangerous clinical decisions.<sup>27</sup> Calibration can be assessed using four levels, with each  
23 level indicating better calibration than the last.<sup>28</sup> The fourth and most stringent level (strong  
24 calibration) requires the correct model to be known, which in turn requires predictors to be non-  
25 continuous, and an infinite amount of data to be used and is therefore considered utopic. We  
26 consider the third level (moderate calibration) using calibration curves. Moderate calibration will  
27 ensure that the model is at least not clinically harmful. Finally, measures of clinical usefulness assess  
28 the clinical consequences of the decision and acknowledge that a false positive may be more or less  
29 severe than a false negative.

30 Firstly, the discriminative performance is assessed using AUROC using the pROC package in R,<sup>29</sup> with  
31 confidence intervals constructed using DeLong's<sup>30</sup> method. For sensitivity, specificity, positive  
32 predictive value (PPV), and negative predictive value (NPV), we use the epiR<sup>31</sup> package in R,<sup>29</sup> with  
33 95% confidence intervals constructed using Jeffrey's prior.<sup>32</sup> We report performance at a range of  
34 probability thresholds to demonstrate how the thresholds can be adjusted to reduce false positives  
35 or false negatives depending on the setting.<sup>33</sup> Secondly, we assess model calibration using  
36 calibration curves created using the CalibrationCurves package,<sup>28</sup> which is based on the rms<sup>34</sup>  
37 package. Finally, we assess the clinical usefulness of the model using decision curve analysis.<sup>35</sup> Net  
38 benefits are given at various thresholds, and models which reach zero net benefit at higher  
39 thresholds are considered more clinically useful. Two brief sensitivity analyses are performed, one  
40 assessing the model's ability to deal with missing data and the other assessing its ability to deal with  
41 noise. To improve the model's interpretability and reduce the black-box nature, we produce saliency  
42 maps<sup>36</sup> that show which areas of the image are helpful to the model in the prediction. We also check  
43 the assumption of normally distributed random-effects parameters.



## 1 Comparison models

2 To assess the added benefit of using our mixed-effects method, we compare against networks that  
3 use alternative methods. Both COVNet<sup>7</sup> and a method proposed by Bai et al.<sup>8</sup> propose deep learning  
4 models that consider the slices separately before concatenating the features using max pooling.  
5 COVNet uses a ResNet50<sup>37</sup> CNN to extract features and pooling layers to concatenate the features  
6 before a fully connected classification layer. The model proposed by Bai et al. uses EfficientNetB4<sup>38</sup>  
7 to extract features followed by a series of full-connected layers with batch normalisation and  
8 dropout; average pooling is then used to concatenate the feature vectors before classification. While  
9 max pooling is simple and computationally efficient, it cannot deal with pose variance and does not  
10 model the relationship between slices.

11 An alternative method to pooling is treating the scans as 3D, such as in CoviNet<sup>39</sup>. CoviNet takes the  
12 whole scan and uses a 16 layer 3D CNN followed by pooling and fully connected layers. We  
13 implemented these models as described in their respective papers.

14 In all comparison experiments, we kept hyperparameters, such as learning rate, learning rate decay,  
15 and data augmentation, the same to ensure the comparisons were fair. For COVNet<sup>7</sup> and the model  
16 proposed by Bai et al.,<sup>8</sup> we pretrained the CNNs on ImageNet as they also did; however, no  
17 pretrained models were available for CoviNet. For the loss function, we also used the Brier score.<sup>24</sup>

## 18 Computing

19 Models were developed using an Amazon Web Services p3.8xlarge node with four Tesla V100 16GiB  
20 GPUs and 244GiB available memory. Model inference was performed on a local Linux machine  
21 running Ubuntu 18.04, with a Titan X 12GiB GPU and 32GiB available memory. Model development  
22 and inference were performed using Tensorflow 2.4,<sup>40,41</sup> and R 4.0.5<sup>29</sup> was used to produce  
23 evaluation metrics<sup>42,43</sup> and graphs.<sup>34,44</sup> We used mixed precision to reduce the computational cost,  
24 which uses 16-bit floating-point precision in all layers, except for the mixed-effects and classification  
25 layers, where 32-bit floating-point precision is used.

26 We used the Adam optimiser<sup>45</sup> with an initial learning rate of 1e-4; if the internal validation loss did  
27 not improve for three epochs, we reduced the learning rate to 20%. In addition, we assumed  
28 convergence and stopped training if the loss did not improve for ten epochs to reduce the time  
29 spent training and the energy used.

## 30 Data

31 There is currently no established method for estimating the sample size estimate in deep learning.  
32 We propose treating the final fully connected classification layer as the model and treating previous  
33 layers as feature extraction. We can then use the number of parameters in the final layer to estimate  
34 the required sample size. Using the 'pmsampsize' package<sup>46</sup> in R, we estimate the required minimum  
35 sample size in the development set. We use a conservative expected C-statistic of 0.8, with 21  
36 parameters and an estimated disease prevalence of 80% based on datasets used in other studies.  
37 This gives a minimum required sample size of 923 patients in the training set. For model validation,  
38 around 200 patients with the disease and 200 patients without the disease are estimated to be  
39 needed to assess calibration.<sup>28</sup>

40 All data used here is retrospectively collected and contains hospital patients with CT scans  
41 performed during the COVID-19 pandemic. The diagnosis was determined by examining radiological  
42 features of the CT scan for signs of COVID-19, such as ground-glass opacities. For model  
43 development, we use the MosMed dataset,<sup>47</sup> which consists of a total of 1,110 CT scans displaying  
44 either healthy or COVID-19 infected lungs. The scans were performed in Moscow hospitals between

1 March 1, 2020, and April 25, 2020. We split the dataset into two sets for training and internal  
2 validation on the patient level. The training set is used to train the model, and the internal validation  
3 set is used to select the best model based on the loss at each epoch; this helps prevent overfitting on  
4 the training set. In addition, we obtained images from a publicly available dataset published by  
5 Zhang et al.<sup>48</sup> consisting of CT images from a consortium of Chinese hospitals.

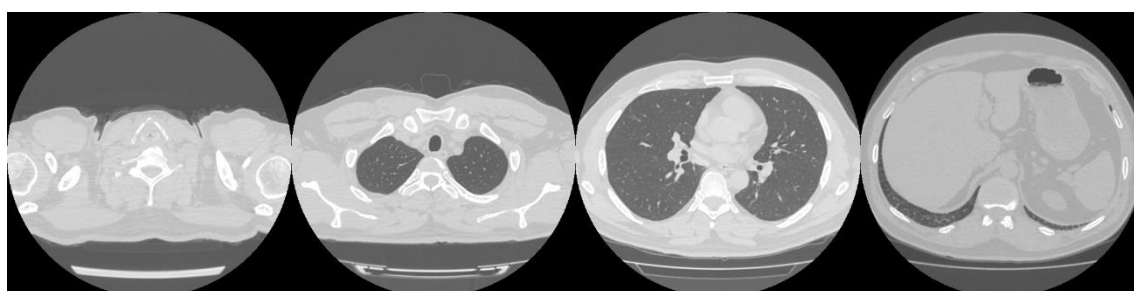
6 Overall, this allows us to perform external geographical validation in another country and to better  
7 evaluate the developed model. In addition, we will be able to assess how well a deep learning model  
8 generalises to other populations. A summary of all the datasets used is shown in Table 1. We have  
9 923 patients in the training set and at least 200 patients in each class for the external validation set.

10 **Table 1:** Summary of the datasets used.

Dataset	Location	Use	Healthy/COVID19
MosMed Training	Moscow, Russia	Training	169/856
MosMed Validation	Moscow, Russia	Internal Validation	85/285
Zhang et al. <sup>48</sup>	China	External Validation	243/553

11

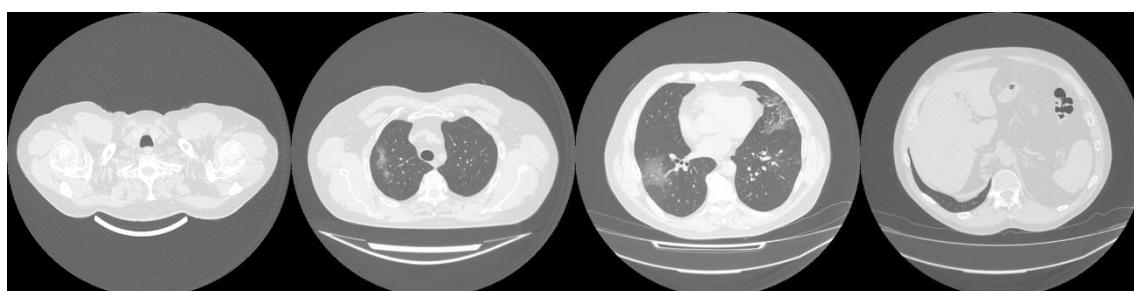
12



13

14

(a)



15

16

(b)

17 **Figure 2:** Example images showing (a) healthy and (b) COVID-19 lungs taken from the Mosmed  
18 dataset.

19 Data pre-processing and augmentation

20 The MosMed dataset was converted from Dicom image format into PNG, normalised to have a mean  
21 of 120 and a variance of 95. Images were ordered from the top of the lungs to the bottom. During  
22 training, we applied random online data augmentation to the images. This alters the image slightly  
23 and gives the effect of increasing the training dataset size, although this is not as good as expanding  
24 the training dataset with more samples. First, we adjusted the brightness and contrast between 80%  
25 and 120%. We then rotated the image plus or minus 5 degrees and cropped the image up to 20% on

1 each side. Finally, we flipped the image horizontally and vertically with a probability of 50% each. All  
2 random values were chosen using the uniform distribution except for the flips, which were chosen  
3 using a random bit.

4 The dataset taken from Zhang et al.<sup>48</sup> required a large amount of sorting to be made suitable for use.  
5 Some of the scans were pre-segmented and only showed the lung areas, while others showed the  
6 whole CT scan. We removed any pre-segmented images. Identifying information on some images  
7 had to be cropped to reduce bias in the algorithm. In addition, many of the scans were duplicates  
8 but were not labelled as such, and many scans were incomplete, only showing a few lung slices or  
9 not showing any lung tissue at all. We only used complete scans with one scan per patient. Finally,  
10 some scans needed to be ordered top to bottom. Using the bilinear sampling algorithm, all images  
11 were resized to 256 by 256 pixels, and image values were divided by 255 to normalise between 0  
12 and 1.

13 The MosMed dataset has a median of 41 slices, a minimum of 31 slices and a maximum of 72 slices.  
14 The Zhang et al. dataset has much greater variability in scan size with a median of 61 slices, a  
15 minimum of 19 slices, and a maximum of 415 slices. We present histograms showing the number of  
16 slices per scan in Figure 3. We require a fixed number of slices as input, and we chose 20 as the slice  
17 size. For all scans, we included the first and last images. If scans had more than 20 slices, we sampled  
18 uniformly to select 20. Only one scan in the Zhang et al. dataset had less than 20 slices; a blank slice  
19 replaced this slice; the mixed-effects model can account for missing data.

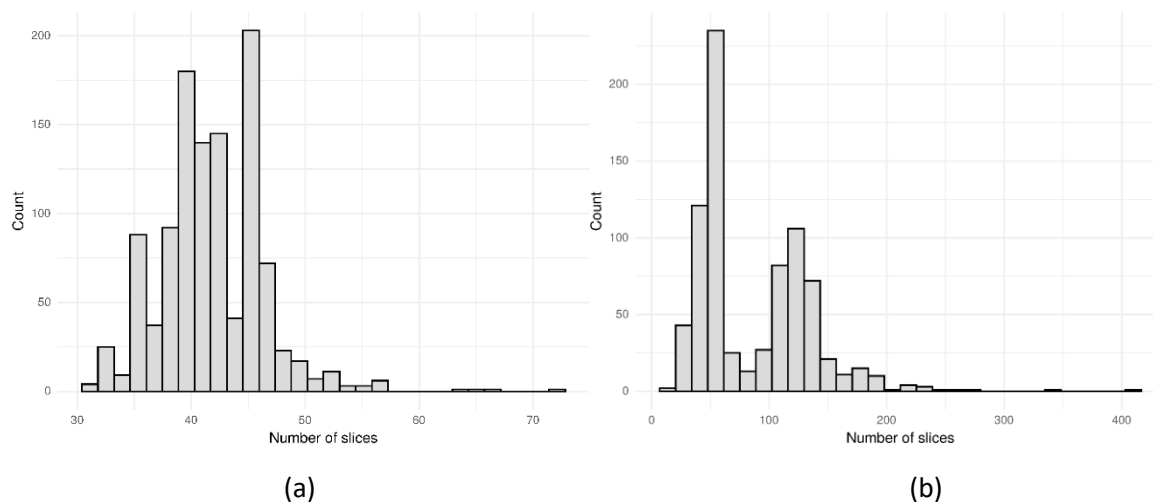


**Figure 3:** Histogram showing the number of slices per scan for (a) the MosMed<sup>47</sup> dataset and (b) the Zhang et al.<sup>48</sup> dataset. The MosMed dataset has much fewer slices on average with a much smaller spread.

## 25 Results

26 On the internal validation dataset, the proposed model attained an AUROC of 0.936 (95%CI: 0.910,  
27 0.961). Using a probability threshold of 0.5, the sensitivity, specificity, NPV, and PPV were 0.753  
28 (0.647, 0.840), 0.909 (0.869, 0.940), 0.711 (0.606, 0.802), and 0.925 (0.888, 0.953), respectively. The  
29 model proposed by Bai et al.<sup>8</sup> attained an AUROC of 0.731 (0.674, 0.80). However, despite attaining  
30 a reasonably AUC value, the model was badly calibrated, and the predicted probabilities of COVID-19  
31 were all clustered around 0.42, meaning that the sensitivity, specificity, PPV, and NPV are  
32 meaningless. We tried to retrain the model and rechecked the code implementation; however, we  
33 could not obtain more meaningful results. Covinet<sup>9</sup> attained an AUROC of 0.810 (0.748, 0.853). Using

1 a probability threshold of 0.5, the sensitivity, specificity, NPV, and PPV were 0.824 (0.726, 0.898),  
2 0.596 (0.537, 0.654), 0.378 (0.308, 0.452), and 0.919 (0.870, 0.954), respectively. COVNet<sup>7</sup> attained  
3 an AUROC of 0.935 (0.912, 0.959). Using a probability threshold of 0.5, the sensitivity, specificity,  
4 NPV, and PPV were 1.0 (0.958, 1.0), 0.796 (0.745, 0.842), 0.594 (0.509, 0.676), and 1.0 (0.984, 1.0),  
5 respectively. Full results for a range of probability thresholds are shown in Table 2.

6 Calibration curves in Figure 5 show reasonable calibration for the mixed-effects model, although the  
7 model may still benefit from some recalibration. The other models do not have good calibration and  
8 likely provide harmful predictions. The decision curve in Figure 6 shows that the proposed model is  
9 of great clinical benefit compared to the treat all and treat-none approach.

10 It is important to remember that the model was selected using this internal testing set to avoid  
11 overfitting on the training set; therefore, these results are biased, and the external validation results  
12 are more representative of the true model performance.

13 On the external geographical validation dataset, the proposed model attained an AUROC of 0.930  
14 (0.914, 0.947). With a probability threshold of 0.5, the sensitivity, specificity, NPV, and PPV were  
15 0.778 (0.720, 0.828), 0.882 (0.853, 0.908), 0.744 (0.686, 0.797), and 0.90 (0.872, 0.924), respectively.  
16 The model proposed by Bai et al.<sup>8</sup> again attained a reasonable AUROC of 0.805 (0.774, 0.836);  
17 however, the sensitivity, specificity, NPV, and PPV were meaningless. Covinet<sup>9</sup> attained an AUROC of  
18 0.651 (0.610, 0.691). Using a probability threshold of 0.5, the sensitivity, specificity, NPV, and PPV  
19 were 0.008 (0.001, 0.029), 0.991 (0.979, 0.997), 0.286 (0.037, 0.710), and 0.695 (0.661, 0.727),  
20 respectively. COVNet<sup>7</sup> attained an AUROC of 0.808 (0.775, 0.841). With a cut-off point of 0.5, the  
21 sensitivity, specificity, NPV, and PPV were 0.387 (0.325, 0.451), 0.940 (0.917, 0.959), 0.740 (0.655,  
22 0.814), and 0.777 (0.744, 0.808), respectively. Full results are shown in Table 3.

23 Similar to the internal validation, Figure 7 shows reasonable calibration for the mixed-effects model,  
24 although some recalibration may improve performance. Again, the comparison models could give  
25 harmful predictions as they are poorly calibrated. The decision curve in Figure 8 shows that the  
26 model is of great clinical benefit compared to the treat all and treat-none approach.

27 Although our proposed method and the Covnet model showed comparable performance on the  
28 internal validation set, the Covnet model could not generalise to the external geographical validation  
29 set, and calibration showed that the Covnet model would provide harmful risk estimates. This  
30 highlights the need for robust external validation in each intended setting. Nevertheless, the results  
31 show that the proposed method better generalises to external geographical datasets and provides  
32 less harmful predictions when compared to the four previously proposed methods based on the  
33 calibration curves.

34

- 1 **Table 2:** Area under the receiver operating characteristic curve (AUROC), sensitivity, specificity, positive predictive value (PPV) and negative predictive value
- 2 (NPV) on the internal validation dataset. Point estimates and 95% confidence intervals were calculated using De Long's method for AUROC and Jeffrey's
- 3 interval for sensitivity, specificity, PPV, and NPV. Results are shown at a range of probability thresholds.

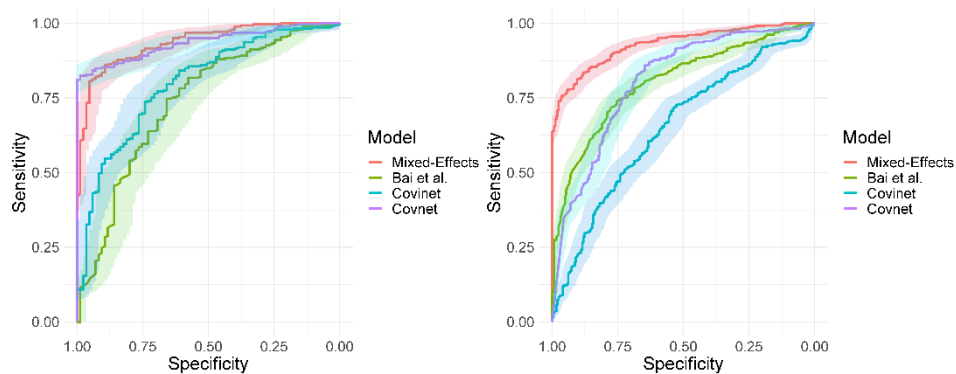
Model	AUROC	Threshold	Sensitivity	Specificity	PPV	NPV
Bai et al	0.731 (0.674, 0.80)	0.3	0.0 (0.0, 0.042)	1.0 (0.987, 1.0)	NA	0.77 (0.724, 0.812)
		0.4	0.012 (0, 0.064)	0.996 (0.981, 1.0)	0.50 (0.013, 0.987)	0.772 (0.725, 0.814)
		0.5	1.0 (0.958, 1.0)	0.0 (0.0, 0.013)	0.230 (0.188, 0.276)	NA
		0.6	1.0 (0.958, 1.0)	0.0 (0.0, 0.013)	0.230 (0.188, 0.276)	NA
		0.7	1.0 (0.958, 1.0)	0.0 (0.0, 0.013)	0.230 (0.188, 0.276)	NA
CoviNet	0.801 (0.748, 0.853)	0.3	0.459 (0.350, 0.570)	0.898 (0.857, 0.931)	0.574 (0.448, 0.693)	0.848 (0.802, 0.886)
		0.4	0.706 (0.597, 0.80)	0.761 (0.708, 0.810)	0.469 (0.380, 0.559)	0.897 (0.851, 0.932)
		0.5	0.824 (0.726, 0.898)	0.596 (0.537, 0.654)	0.378 (0.308, 0.452)	0.919 (0.870, 0.954)
		0.6	0.918 (0.838, 0.966)	0.446 (0.387, 0.505)	0.331 (0.271, 0.394)	0.948 (0.895, 0.979)
		0.7	0.965 (0.90, 0.993)	0.246 (0.197, 0.30)	0.276 (0.226, 0.331)	0.959 (0.885, 0.991)
CovNet	0.935 (0.912, 0.959)	0.3	0.941 (0.868, 0.981)	0.839 (0.791, 0.879)	0.635 (0.544, 0.719)	0.98 (0.953, 0.993)
		0.4	0.965 (0.90, 0.993)	0.825 (0.775, 0.867)	0.621 (0.533, 0.704)	0.987 (0.964, 0.997)
		0.5	1.0 (0.958, 1.0)	0.796 (0.745, 0.842)	0.594 (0.509, 0.676)	1.0 (0.984, 1.0)
		0.6	1.0 (0.958, 1.0)	0.779 (0.726, 0.826)	0.574 (0.490, 0.655)	1.0 (0.984, 1.0)
		0.7	1.0 (0.958, 1.0)	0.761 (0.708, 0.810)	0.556 (0.473, 0.636)	1.0 (0.984, 1.0)
Mixed-Effects (Ours)	0.936 (0.910, 0.961)	0.3	0.588 (0.476, 0.694)	0.961 (0.932, 0.981)	0.820 (0.70, 0.906)	0.887 (0.846, 0.920)
		0.4	0.659 (0.548, 0.758)	0.933 (0.898, 0.959)	0.747 (0.633, 0.840)	0.902 (0.862, 0.933)
		0.5	0.753 (0.647, 0.840)	0.909 (0.869, 0.940)	0.711 (0.606, 0.802)	0.925 (0.888, 0.953)
		0.6	0.812 (0.712, 0.888)	0.884 (0.841, 0.919)	0.676 (0.577, 0.766)	0.940 (0.905, 0.960)
		0.7	0.906 (0.823, 0.958)	0.832 (0.783, 0.873)	0.616 (0.525, 0.702)	0.967 (0.937, 0.986)

1 **Table 3:** Area under the receiver operating characteristic curve (AUROC), sensitivity, specificity, positive predictive value (PPV) and negative predictive value  
2 (NPV) on the external validation dataset. Point estimates and 95% confidence intervals were calculated using De Long's method for AUROC and Jeffrey's  
3 interval for sensitivity, specificity, PPV, and NPV. Results are shown at a range of probability thresholds.

4

Model	AUROC	Threshold	Sensitivity	Specificity	PPV	NPV
Bai et al	0.805 (0.774, 0.836)	0.3	0.0 (0.0, 0.015)	1.0 (0.993, 1.0)	NA	0.695 (0.661, 0.727)
		0.4	0.0 (0.0, 0.015)	1.0 (0.993, 1.0)	NA	0.695 (0.661, 0.727)
		0.5	1.0 (0.985, 1.0)	1.0 (0.0, 0.007)	0.305 (0.273, 0.339)	NA
		0.6	1.0 (0.985, 1.0)	1.0 (0.0, 0.007)	0.305 (0.273, 0.339)	NA
		0.7	1.0 (0.985, 1.0)	1.0 (0.0, 0.007)	0.305 (0.273, 0.339)	NA
CoviNet	0.651 (0.610, 0.691)	0.3	0.0 (0.0, 0.015)	1.0 (0.993, 1.0)	NA	0.695 (0.661, 0.727)
		0.4	0.0 (0.0, 0.015)	1.0 (0.993, 1.0)	NA	0.695 (0.661, 0.727)
		0.5	0.008 (0.001, 0.029)	0.991 (0.979, 0.997)	0.286 (0.037, 0.710)	0.695 (0.661, 0.727)
		0.6	0.160 (0.117, 0.213)	0.929 (0.905, 0.949)	0.50 (0.385, 0.615)	0.716 (0.681, 0.749)
		0.7	0.551 (0.487, 0.615)	0.694 (0.654, 0.733)	0.442 (0.385, 0.50)	0.779 (0.740, 0.815)
CovNet	0.808 (0.775, 0.841)	0.3	0.305 (0.247, 0.367)	0.969 (0.951, 0.982)	0.813 (0.718, 0.887)	0.760 (0.727, 0.791)
		0.4	0.354 (0.294, 0.418)	0.955 (0.934, 0.971)	0.775 (0.686, 0.849)	0.771 (0.737, 0.802)
		0.5	0.387 (0.325, 0.451)	0.940 (0.917, 0.959)	0.740 (0.655, 0.814)	0.777 (0.744, 0.808)
		0.6	0.432 (0.369, 0.497)	0.937 (0.913, 0.956)	0.750 (0.670, 0.819)	0.790 (0.756, 0.820)
		0.7	0.473 (0.409, 0.538)	0.931 (0.907, 0.951)	0.752 (0.675, 0.818)	0.801 (0.768, 0.831)
Mixed-Effects (Ours)	0.930 (0.914, 0.947)	0.3	0.675 (0.612, 0.733)	0.935 (0.911, 0.954)	0.820 (0.760, 0.871)	0.867 (0.838, 0.894)
		0.4	0.741 (0.681, 0.795)	0.904 (0.877, 0.927)	0.773 (0.713, 0.825)	0.888 (0.859, 0.913)
		0.5	0.778 (0.720, 0.828)	0.882 (0.853, 0.908)	0.744 (0.686, 0.797)	0.90 (0.872, 0.924)
		0.6	0.827 (0.774, 0.873)	0.859 (0.827, 0.887)	0.720 (0.664, 0.772)	0.919 (0.892, 0.941)
		0.7	0.885 (0.838, 0.922)	0.828 (0.794, 0.859)	0.694 (0.639, 0.744)	0.942 (0.918, 0.961)

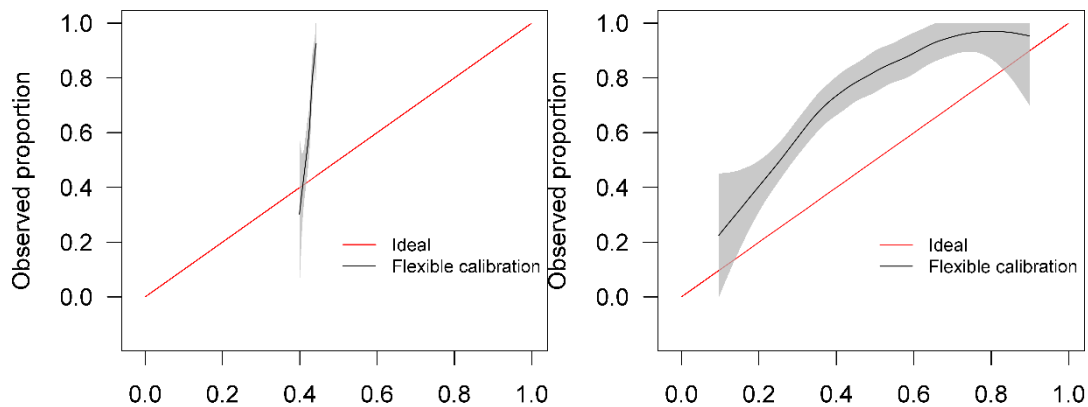
1



2

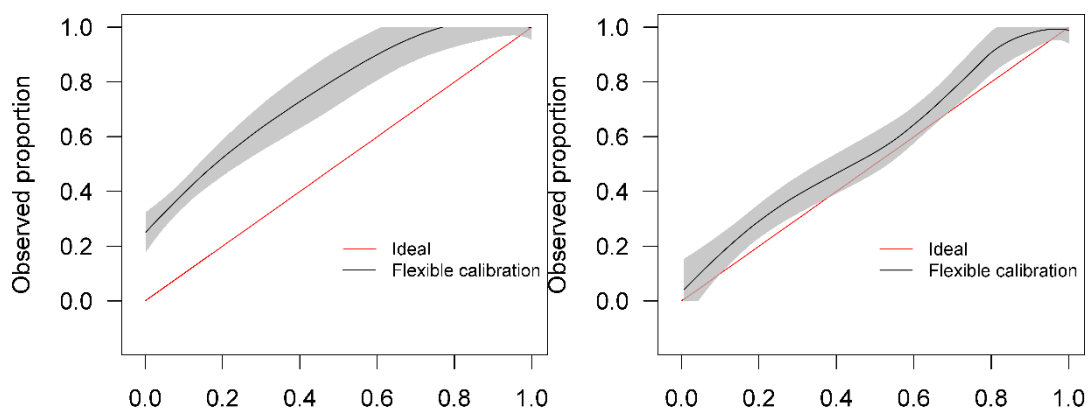
3

4 **Figure 4:** Receiver operating characteristic curves for (a) the MosMed internal validation set and (b)  
5 the Zhang et al.<sup>48</sup> external validation set.



6

7

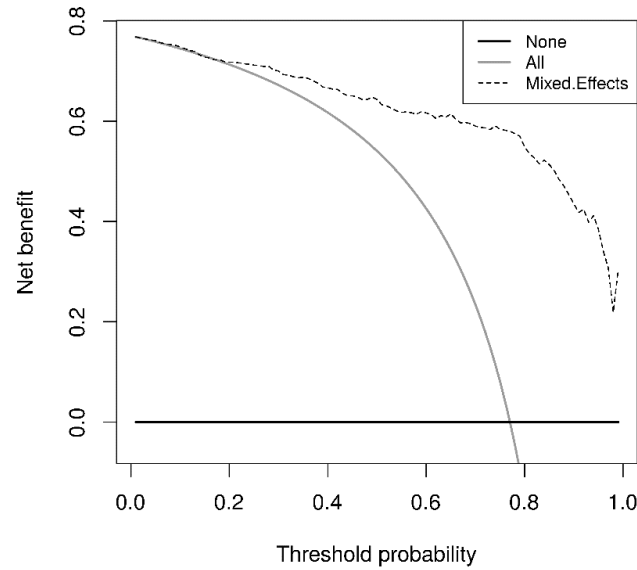


8

9

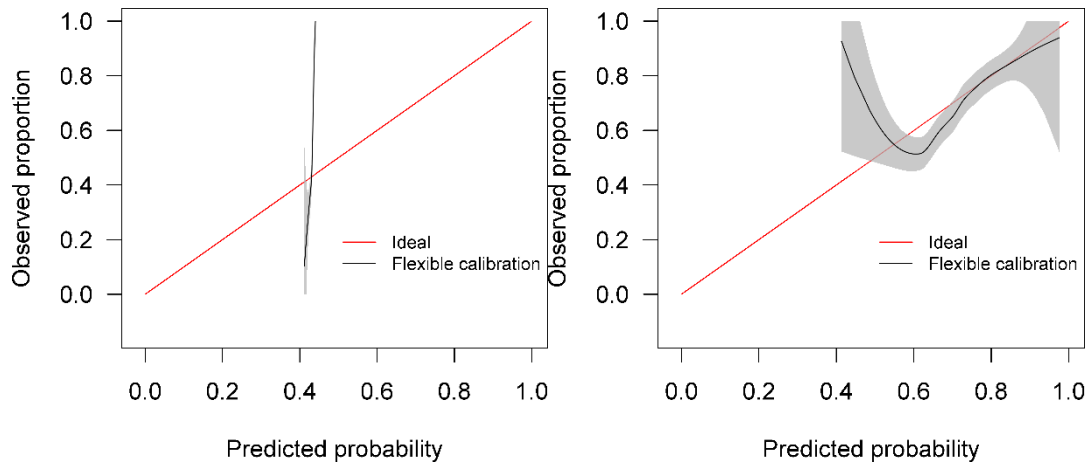
10 **Figure 5:** Calibration curves for (a) the Bai et al.<sup>8</sup> model (b) the Covinet model<sup>9</sup>, (c) the Covnet  
11 model<sup>7</sup>, (d) the proposed mixed-effects model on the Mosmed internal validation dataset.





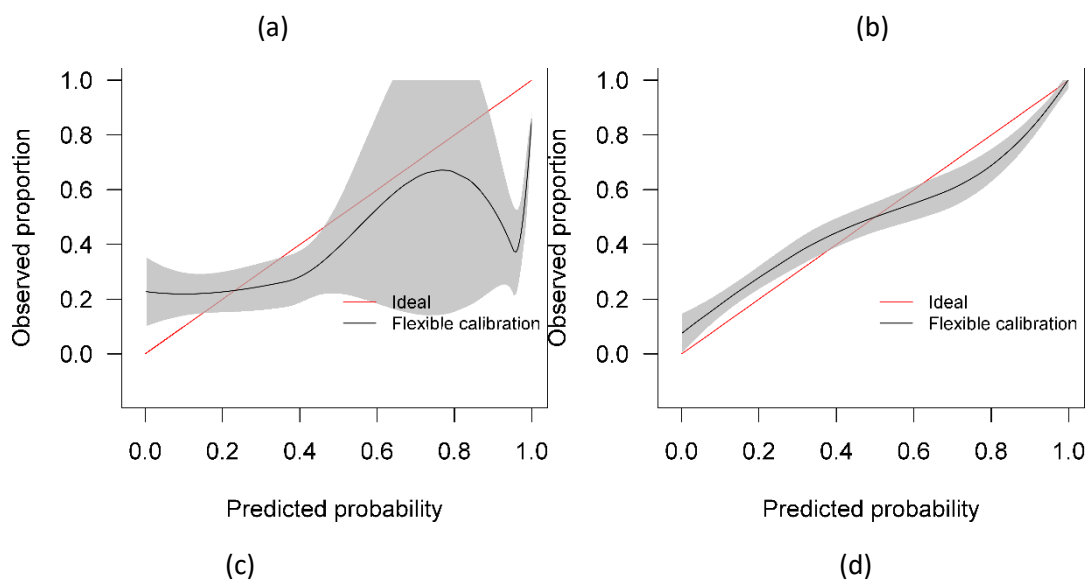
1

2 **Figure 6:** Decision curves for the proposed mixed-effects model on the Mosmed internal validation  
3 dataset.



4

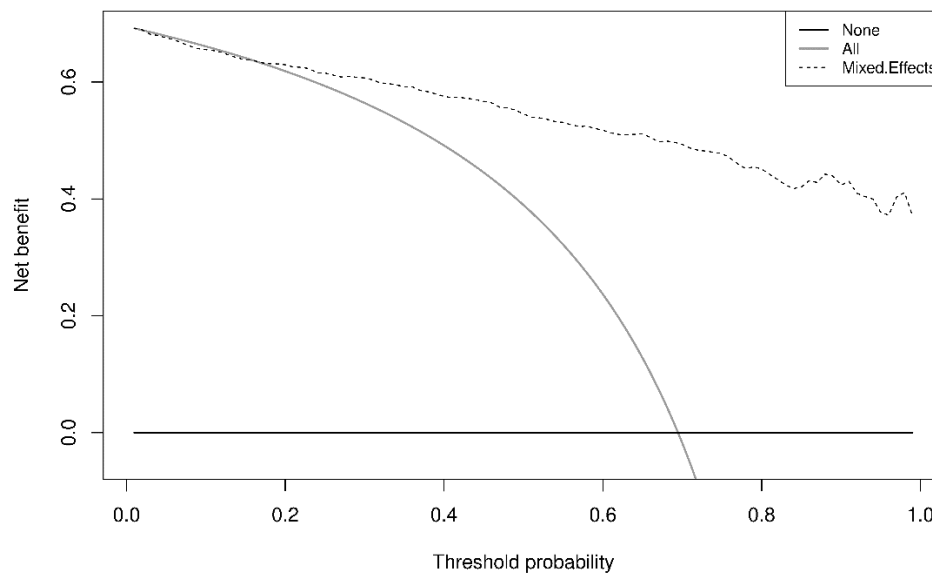
5



6

7

8 **Figure 7:** Calibration curves for (a) the Bai et al.<sup>8</sup> model (b) the Covinet model<sup>9</sup>, (c) the Covnet  
9 model<sup>7</sup>, (d) the proposed mixed-effects model on the Zhang et al. external validation dataset.



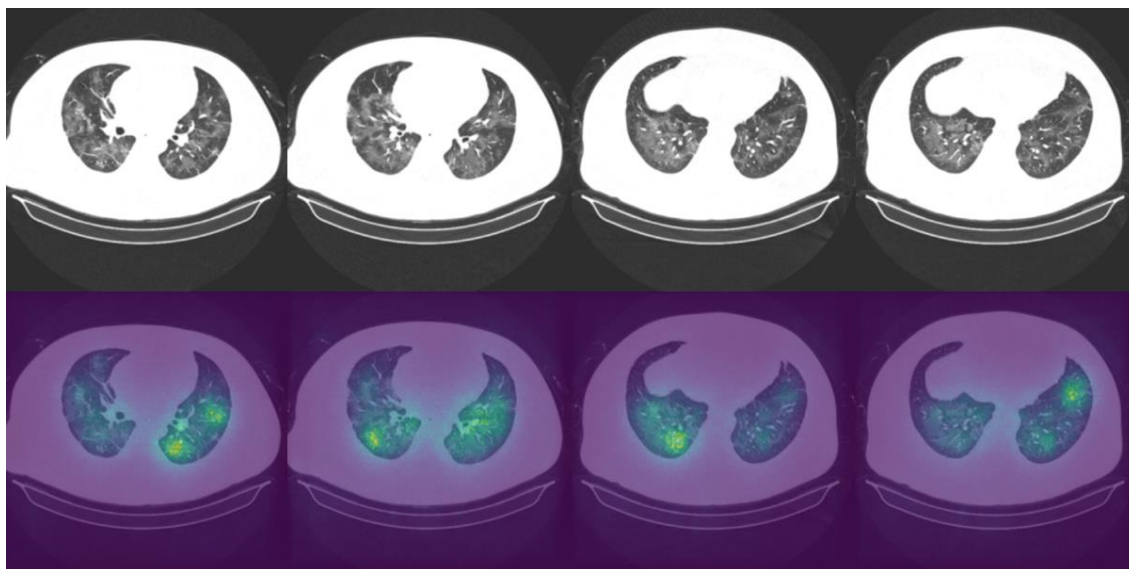
1

2 **Figure 8:** Decision curves for the proposed mixed-effects model on the Zhang et al. external  
3 validation dataset.

4 Saliency maps

5 It is vital to understand how the algorithm makes decisions and to check that it identifies the correct  
6 features within the image. Saliency maps can be used as a visual check to see what features the  
7 algorithm is learning. For example, the saliency maps in Figure 9 show that the model correctly  
8 identifies the diseased areas of the scans. We used 100 samples with a smoothing noise of 0.05 to  
9 create these saliency maps.

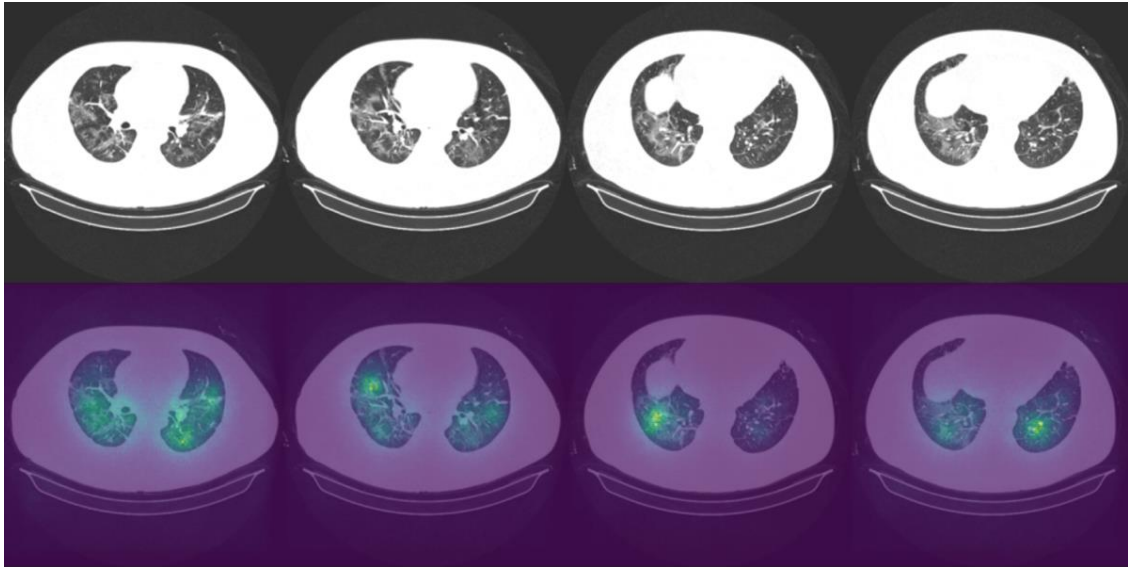
10



11

12

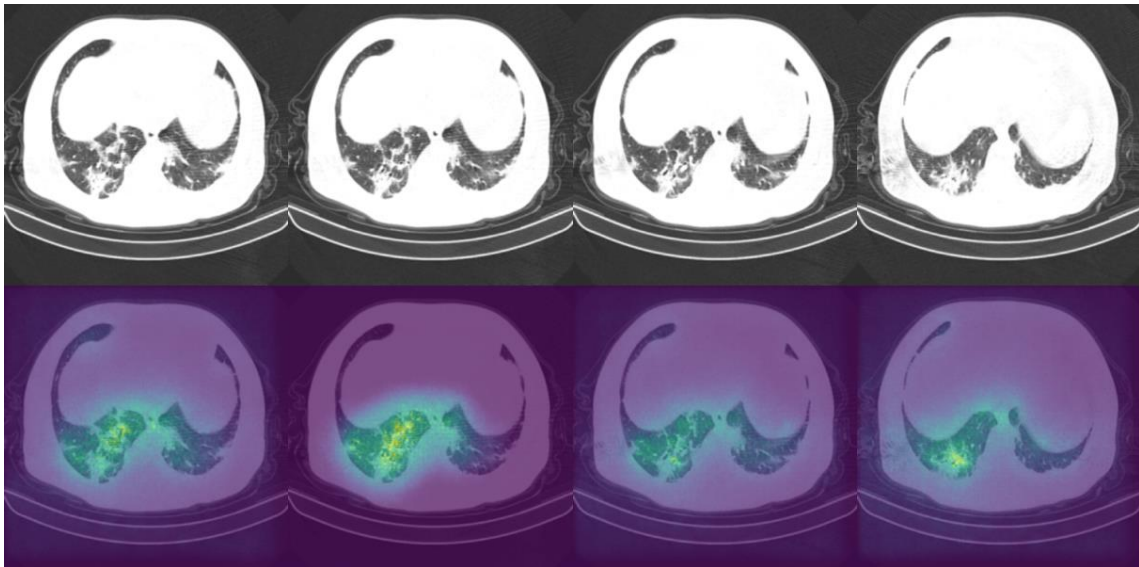
(a)



1

2

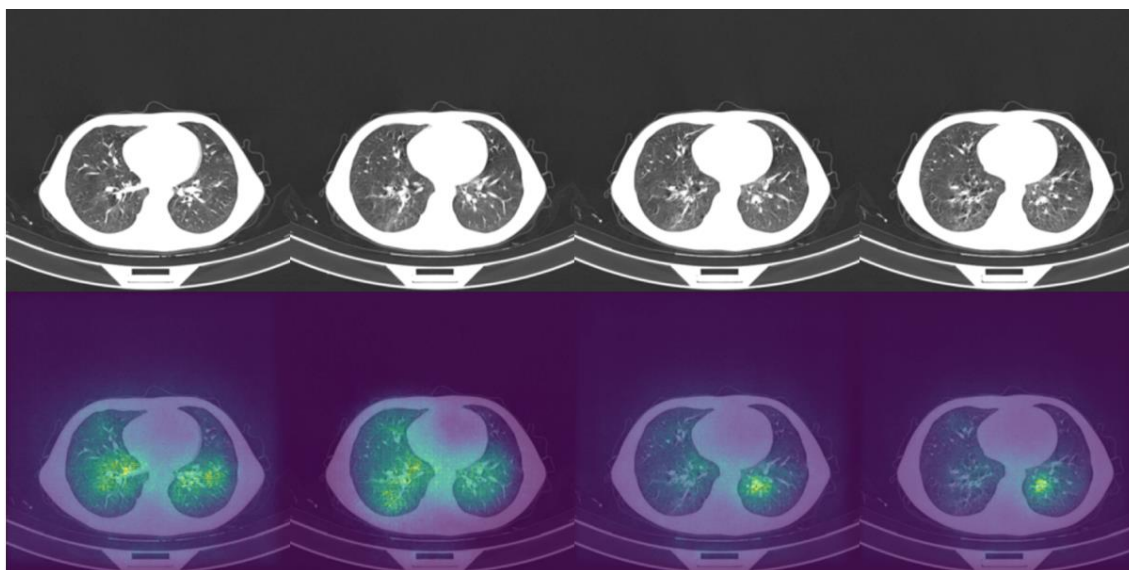
(b)



3

4

(c)



1

2

(d)

3 **Figure 9:** Example of original images and saliency maps showing highlighted regions on four patients  
4 (a, b, c, and d) in the Zhang et al.<sup>48</sup> dataset. Four consecutive slices display how the diseased areas  
5 differ between slices. All images are taken from the external validation set.

6 Sensitivity analysis

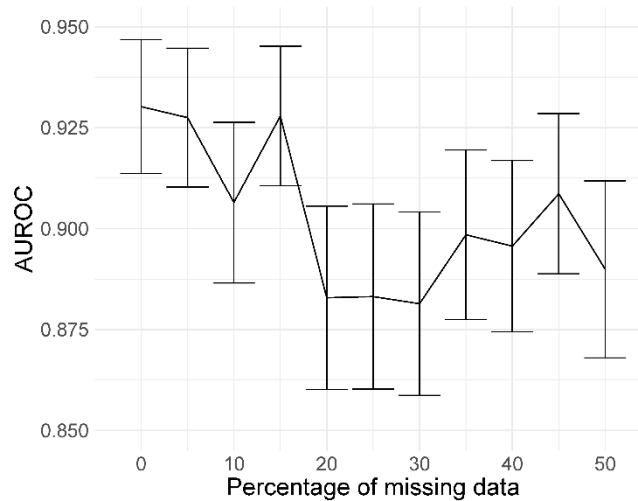
7 Mixed-effects models are capable of accounting for missing data. However, only one image had less  
8 than 20 slices; hence, we could not adequately assess if our model can indeed maintain good  
9 performance with missing data. Here, we rerun the analysis using the same dataset, using the same  
10 model and weights; however, we reduce the number of slices available as testing data inputs to  
11 simulate missing data. Blank images replace these slices. We uniformly sampled the slices choosing  
12 between 10 and 19 slices; this equates to between 5 and 50% missing data for the model. We ran  
13 inference at each level of missingness and briefly show the AUROC to determine at which point the  
14 predictive performance is significantly reduced.

15 The plot of AUROCs at different levels of missingness is shown in Figure 10, along with 95%  
16 confidence intervals. We can see that at 20% missingness, there is a statistically significant decrease  
17 in predictive performance. Although, even at 50% missingness, the model still performs relatively  
18 well, with an AUROC of 0.890 (95% CI: 0.868, 0.912). It should be noted that this does not mean that  
19 there is no reduction in performance at 5-15% missingness, only that the reduction was not  
20 statistically significant at the 95% confidence level.

21 Deep learning models can be susceptible to adversarial attacks<sup>49</sup>, where minor artefacts or noise on  
22 an image can cause the image to be misclassified, even when the image does not look significantly  
23 different to a human observer. Here, we perform a brief sensitivity analysis by adding a small  
24 Gaussian noise to the image. We tested the model performance on the external dataset, with each  
25 image having a random Gaussian noise added. Experiments were conducted with standard  
26 deviations of 0 up to 0.005 in increments of 0.001 added to the normalised image. We did not add  
27 Gaussian noise in the data augmentation so that the model is not explicitly trained to deal with this  
28 kind of attack.

29 When using a variance of 0, the images are unchanged, and the results are the same as the standard  
30 results above. We present results on the Zhang et al.<sup>48</sup> dataset. Example images for each level of  
31 variance are shown in Figure 11, and a graph showing the reduction in AUROC is shown in Figure 12.

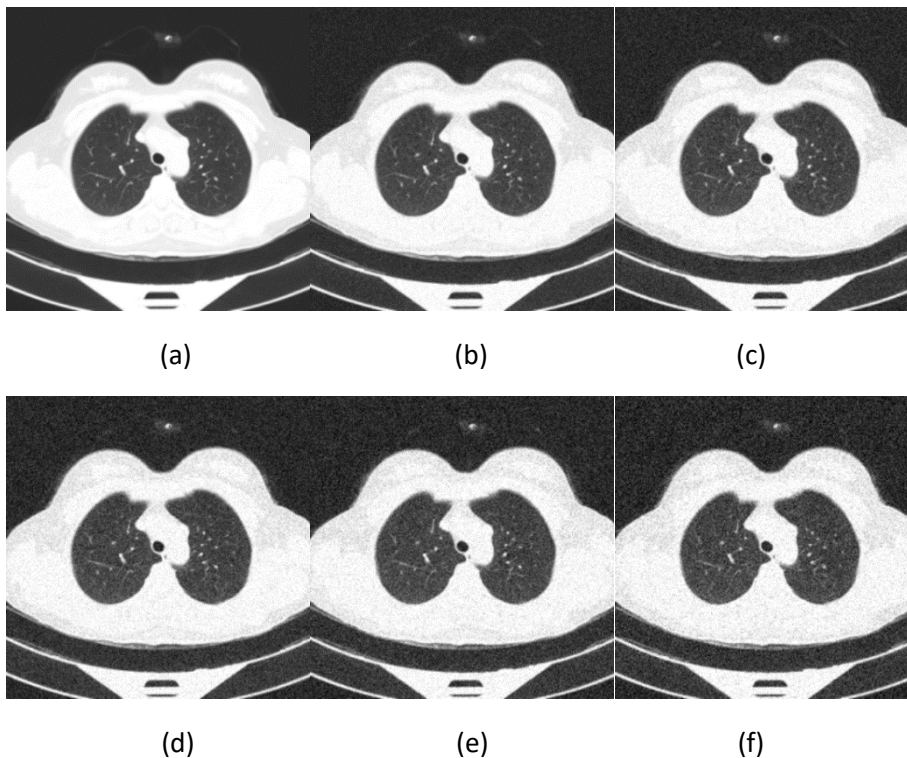
1



2

3 **Figure 10:** AUROC values at different levels of missingness. At 20% missingness, the loss in  
4 performance becomes statistically significant; however, even with 50% missing images, the model  
5 still has a reasonably high AUROC.

6



7

8

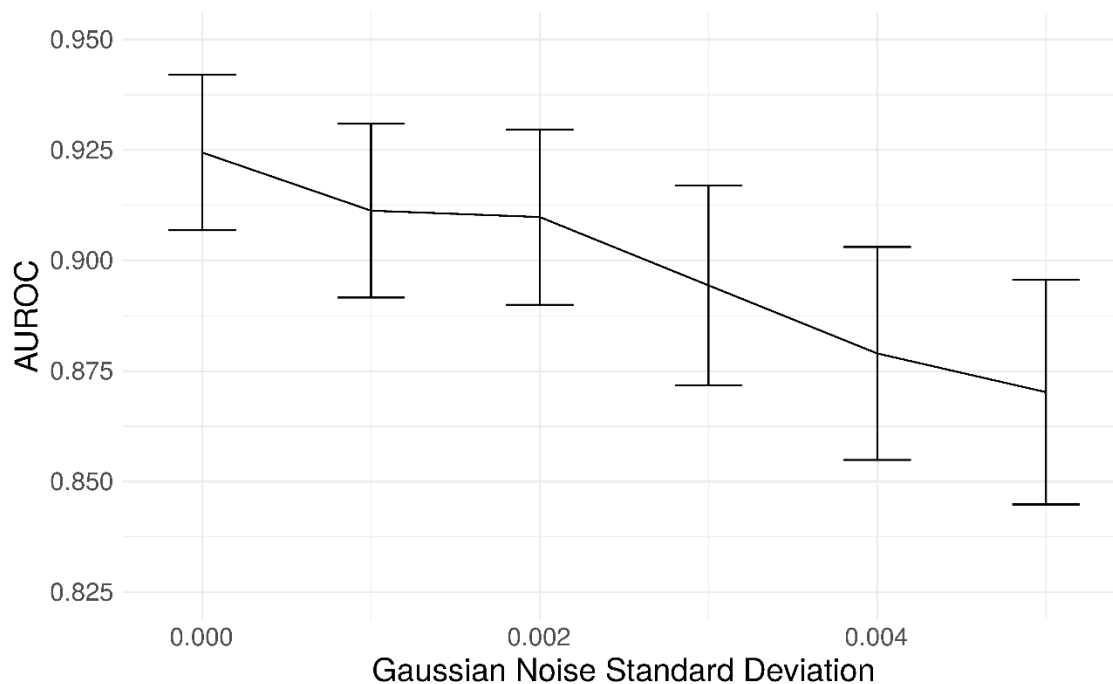
9

10

11 **Figure 11:** Example images showing the effect of increasing the amount of noise in the image input.  
12 Noise is increased by increasing the standard deviation (s.d.) of the Gaussian noise. (a) s.d.=0; (b)  
13 s.d.=0.001; (c) s.d.=0.002; (d) s.d.=0.003; (e) s.d.=0.004; (f) s.d.=0.005.

14





1  
2 **Figure 12:** Graph showing the drop in AUROC as the amount of noise in the image input increases.  
3 The AUROC falls steadily with increased noise in the image.

#### 4 Discussion

5 Artificial intelligence is set to revolutionise healthcare, allowing large amounts of data to be  
6 processed and analysed automatically, reducing pressure on stretched healthcare services. These  
7 tools can aid clinicians in monitoring and managing both common conditions and outbreaks of novel  
8 diseases. However, these tools must be assessed adequately, and best practice guidelines for  
9 reporting and development must be followed closely to increase reproducibility and reduce bias. We  
10 have developed a deep learning model to classify CT scans as healthy or COVID-19 using a novel  
11 mixed-effects model. Following best practice guidelines, we have externally validated the model. In  
12 addition, we robustly externally geographically validated the developed model in several  
13 performance areas, which are not routinely reported. For example, discriminative performance  
14 measures show that the model can discriminate between healthy and COVID-19 CT scans well,  
15 calibration shows that the model is not clinically harmful. Finally, the clinical usefulness measures  
16 show that the model may be useful in a clinical setting. From the results presented here, it would  
17 seem that our deep learning model outperforms the RT-PCR tests as shown in the review by Watson  
18 et al.<sup>3</sup>; however, those results are conservative estimates and were conducted under real-world  
19 clinical settings. A prospective study is required to determine if this is the case.

20 Compared to previously proposed models, our model showed similar discriminative performance to  
21 one existing method; however, our method generalised better to an external geographical validation  
22 set and showed improved calibration performance. Interestingly, in both internal and external  
23 validation, the sensitivity and NPV are similar in all models. However, the specificity and PPV are  
24 statistically significantly improved for the mixed-effects model in the external validations dataset.  
25 The performance of the proposed model in the external validation set is similar to that reported by  
26 PCR testing<sup>3</sup>. However, a direct comparison should not be made as PCR testing on this exact dataset  
27 is unavailable.

1 There are several limitations of the study that should be highlighted and improved in future work.  
2 Firstly, we have only performed external geographical validation in a single dataset. Further external  
3 validation, both geographical and temporal, is needed on many datasets to determine if the model is  
4 correct in each intended setting. Although we performed a brief sensitivity analysis here, more  
5 extensive work on adversarial attacks is needed. Future studies could consider following the method  
6 proposed by Goodfellow et al.<sup>49</sup> to improve robustness against adversarial examples. Patient  
7 demographic data were not available for this study, but future studies could incorporate this data  
8 into the model to improve results. Finally, rules of thumb for assessing sample size calculations in  
9 the validation set can lead to imprecise results<sup>50</sup>. Simulating data is a better alternative; however, it  
10 is difficult to anticipate the distribution of the model's linear predictor. Therefore, we were required  
11 to revert to the rule of thumb using a minimum of 200 samples in each group<sup>28</sup>.

12 Initial experiments used the Zhang et al.<sup>48</sup> dataset for training; this showed promising results on the  
13 internal validation set; however, external validation showed random results. In addition, saliency  
14 maps showed that the model was not using the features of COVID-19 to make the diagnosis and was  
15 instead using the area around the image. We concluded that the images for each class were slightly  
16 different, perhaps due to different imaging protocols, and the algorithm was learning the image  
17 format rather than the disease. We then used the MosMed dataset for training and the Zhang et  
18 al.<sup>48</sup> dataset for external validation. This highlights the need for good quality training data and  
19 external validation and visualisation.

20 Future studies should validate models and follow reporting guidelines such as TRIPOD<sup>17</sup> or the  
21 upcoming QUADAD-AI<sup>51</sup> and TRIPOD-AI<sup>52</sup> to bring about clinically useful and deployable models.  
22 Further research could look deeper into the areas of images identified by the algorithm as shown on  
23 the saliency maps; this could potentially identify new features of COVID-19 which have gone  
24 unnoticed. Before any model can be fully deployed, clinical trials are needed to study the full impact  
25 of using such algorithms to diagnose COVID-19 and the exact situations in which such a model may  
26 be used. In-clinic prospective studies comparing the performance deep learning models with RT-PCR  
27 and lateral flow tests should be carried out to determine how deep learning compares; this will show  
28 whether deep learning could be used as an automated alternative to RT-PCR testing.

29 This study indicates that deep learning could be suitable for screening and monitoring of COVID-19  
30 in a clinical setting; however, validation in the intended setting is vital, and models should not be  
31 adopted without this. It has been observed that the quality of reporting of deep learning prediction  
32 models is usually very poor; however, with a bit of extra work and by following best practice  
33 guidelines, this problem can be overcome. This study highlights the importance of robust analysis  
34 and reporting of models with external validation.

35

## 36 References

- 37 1. Coronavirus disease 2019 (COVID-19) - Symptoms, diagnosis and treatment | BMJ Best Practice:  
38 BMJ Publishing Group; 2020 [Available from: [https://bestpractice.bmj.com/topics/en-](https://bestpractice.bmj.com/topics/en-gb/3000201)  
39 [gb/3000201](https://bestpractice.bmj.com/topics/en-gb/3000201)].
- 40 2. Torjesen I. Covid-19 will become endemic but with decreased potency over time, scientists  
41 believe. *BMJ* 2021;372:n494. doi: 10.1136/bmj.n494
- 42 3. Watson J, Whiting PF, Brush JE. Interpreting a covid-19 test result. *BMJ* 2020;369:m1808. doi:  
43 10.1136/bmj.m1808



- 1 4. Mallett S, Allen AJ, Graziadio S, et al. At what times during infection is SARS-CoV-2 detectable and  
2 no longer detectable using RT-PCR-based tests? A systematic review of individual participant  
3 data. *BMC Medicine* 2020;18(1):346. doi: 10.1186/s12916-020-01810-8
- 4 5. Ruan Z-R, Gong P, Han W, et al. A case of coronavirus disease 2019 with twice negative nucleic  
5 acid testing within 8 days. *Chinese Medical Journal* 2020;133(12)
- 6 6. Pontone G, Scafuri S, Mancini ME, et al. Role of computed tomography in COVID-19. *J Cardiovasc*  
7 *Comput Tomogr* 2020:S1934-5925(20)30436-6. doi: 10.1016/j.jcct.2020.08.013
- 8 7. Li L, Qin L, Xu Z, et al. Using Artificial Intelligence to Detect COVID-19 and Community-acquired  
9 Pneumonia Based on Pulmonary CT: Evaluation of the Diagnostic Accuracy. *Radiology*  
10 2020;296(2):E65-E71. doi: 10.1148/radiol.2020200905
- 11 8. Bai HX, Wang R, Xiong Z, et al. Artificial Intelligence Augmentation of Radiologist Performance in  
12 Distinguishing COVID-19 from Pneumonia of Other Origin at Chest CT. *Radiology*  
13 2020;296(3):E156-E65. doi: 10.1148/radiol.2020201491
- 14 9. Mittal B, Oh J. CoviNet: Covid-19 diagnosis using machine learning analyses for computerized  
15 tomography images. *Thirteenth International Conference on Digital Image Processing (ICDIP*  
16 *2021)* 2021;11878:1187816.
- 17 10. MacCormick IJC, Zheng Y, Czanner S, et al. Spatial statistical modelling of capillary non-perfusion  
18 in the retina. *Scientific Reports* 2017;7(1):16792. doi: 10.1038/s41598-017-16620-x
- 19 11. Zhu W, Ku JY, Zheng Y, et al. Spatial linear mixed effects modelling for OCT images: SLME model.  
20 *Journal of Imaging* 2020;6(6):44.
- 21 12. Albtoush OM, Al-Shdefat RB, Al-Akaileh A. Chest CT scan features from 302 patients with COVID-  
22 19 in Jordan. *European Journal of Radiology Open* 2020;7:100295. doi:  
23 <https://doi.org/10.1016/j.ejro.2020.100295>
- 24 13. Haseli S, Khalili N, Bakhshayeshkaram M, et al. Lobar distribution of COVID-19 pneumonia based  
25 on chest computed tomography findings; A retrospective study. *Arch Acad Emerg Med*  
26 2020;8(1):e55-e55.
- 27 14. Xiang C, Lu J, Zhou J, et al. CT findings in a novel coronavirus disease (COVID-19) pneumonia at  
28 initial presentation. *BioMed Research International* 2020;2020:5436025. doi:  
29 10.1155/2020/5436025
- 30 15. Wynants L, Van Calster B, Collins GS, et al. Prediction models for diagnosis and prognosis of  
31 covid-19: systematic review and critical appraisal. *BMJ* 2020;369:m1328. doi:  
32 10.1136/bmj.m1328
- 33 16. Roberts M, Driggs D, Thorpe M, et al. Common pitfalls and recommendations for using machine  
34 learning to detect and prognosticate for COVID-19 using chest radiographs and CT scans.  
35 *Nature Machine Intelligence* 2021;3(3):199-217. doi: 10.1038/s42256-021-00307-0
- 36 17. Collins GS, Reitsma JB, Altman DG, et al. Transparent reporting of a multivariable prediction  
37 model for individual prognosis or diagnosis (TRIPOD): the TRIPOD statement. *BMJ : British*  
38 *Medical Journal* 2015;350:g7594. doi: 10.1136/bmj.g7594
- 39 18. Mongan J, Moy L, Kahn CE. Checklist for artificial intelligence in medical imaging (CLAIM): A guide  
40 for authors and reviewers. *Radiology: Artificial Intelligence* 2020;2(2):e200029. doi:  
41 10.1148/ryai.2020200029
- 42 19. Wolff RF, Moons KGM, Riley RD, et al. PROBAST: A tool to assess the risk of bias and applicability  
43 of prediction model studies. *Annals of Internal Medicine* 2019;170(1):51-58. doi:  
44 10.7326/M18-1376
- 45 20. Jiang J, Nguyen T. Linear and generalized linear mixed models and their applications: Springer  
46 2007.
- 47 21. Szegedy C, Vanhoucke V, Ioffe S, et al. Rethinking the inception architecture for computer vision.  
48 *Proceedings of the IEEE conference on computer vision and pattern recognition* 2016:2818-  
49 26.

- 1 22. Deng J, Dong W, Socher R, et al. ImageNet: A large-scale hierarchical image database. *2009 IEEE*  
2 *Conference on Computer Vision and Pattern Recognition 2009*:248-55. doi:  
3 10.1109/CVPR.2009.5206848
- 4 23. Xiong Y, Kim HJ, Singh V. Mixed effects neural networks (MeNets) with applications to gaze  
5 estimation. *2019 IEEE/CVF Conference on Computer Vision and Pattern Recognition (CVPR)*  
6 2019:7735-44. doi: 10.1109/CVPR.2019.00793
- 7 24. Brier GW. VERIFICATION OF FORECASTS EXPRESSED IN TERMS OF PROBABILITY. *Monthly*  
8 *Weather Review* 1950;78(1):1-3. doi: 10.1175/1520-0493(1950)078<0001:VOFEIT>2.0.CO;2
- 9 25. Platt J. Probabilistic outputs for support vector machines and comparisons to regularized  
10 likelihood methods. *Advances in large margin classifiers* 1999;10(3):61-74.
- 11 26. Steyerberg EW, Vickers AJ, Cook NR, et al. Assessing the performance of prediction models: A  
12 framework for traditional and novel measures. *Epidemiology* 2010;21(1)
- 13 27. Van Calster B, McLernon DJ, van Smeden M, et al. Calibration: the Achilles heel of predictive  
14 analytics. *BMC Medicine* 2019;17(1):230. doi: 10.1186/s12916-019-1466-7
- 15 28. Van Calster B, Nieboer D, Vergouwe Y, et al. A calibration hierarchy for risk models was defined:  
16 from utopia to empirical data. *Journal of Clinical Epidemiology* 2016;74:167-76. doi:  
17 <https://doi.org/10.1016/j.jclinepi.2015.12.005>
- 18 29. R: A Language and Environment for Statistical Computing [program], 2021.
- 19 30. DeLong ER, DeLong DM, Clarke-Pearson DL. Comparing the Areas under Two or More Correlated  
20 Receiver Operating Characteristic Curves: A Nonparametric Approach. *Biometrics*  
21 1988;44(3):837-45. doi: 10.2307/2531595
- 22 31. Stevenson M, Sergeant E, Nunes T, et al. epiR: Tools for the Analysis of Epidemiological Data.  
23 2022 doi: <https://CRAN.R-project.org/package=epiR>
- 24 32. Brown LD, Cai TT, DasGupta A. Interval Estimation for a Binomial Proportion. *Statistical Science*  
25 2001;16(2):101-17.
- 26 33. Wynants L, van Smeden M, McLernon DJ, et al. Three myths about risk thresholds for prediction  
27 models. *BMC Medicine* 2019;17(1):192. doi: 10.1186/s12916-019-1425-3
- 28 34. rms: Regression Modeling Strategies [program], 2021.
- 29 35. Vickers AJ, Elkin EB. Decision curve analysis: a novel method for evaluating prediction models.  
30 *Med Decis Making* 2006;26(6):565-74. doi: 10.1177/0272989X06295361
- 31 36. Smilkov D, Thorat N, Kim B, et al. Smoothgrad: Removing noise by adding noise. arXiv 2017. *arXiv*  
32 *preprint arXiv:170603825*
- 33 37. He K, Zhang X, Ren S, et al. Deep residual learning for image recognition. *Proceedings of the IEEE*  
34 *conference on computer vision and pattern recognition* 2016:770-78.
- 35 38. Efficientnet: Rethinking model scaling for convolutional neural networks. International  
36 Conference on Machine Learning; 2019. PMLR.
- 37 39. Mittal B, Oh J. CoviNet: Covid-19 diagnosis using machine learning analyses for computerized  
38 tomography images. *ProcSPIE* 2021;11878 doi: 10.1117/12.2601065
- 39 40. Abadi M, Agarwal A, Barham P, et al. Tensorflow: Large-scale machine learning on  
40 heterogeneous distributed systems. *arXiv preprint arXiv:160304467* 2016
- 41 41. Tensorflow: A system for large-scale machine learning. 12th {USENIX} symposium on operating  
42 systems design and implementation ({OSDI} 16); 2016.
- 43 42. Robin X, Turck N, Hainard A, et al. pROC: an open-source package for R and S+ to analyze and  
44 compare ROC curves. *BMC Bioinformatics* 2011;12(1):77. doi: 10.1186/1471-2105-12-77
- 45 43. Du Z, Hao Y. reportROC: an easy way to report ROC analysis. R package version 3.5, 2020.
- 46 44. Wickham H. ggplot2: Elegant Graphics for Data Analysis.: Springer-Verlag New York 2016.
- 47 45. Kingma DP, Ba J. Adam: A method for stochastic optimization. *arXiv preprint arXiv:1412.6980*  
48 2014
- 49 46. Riley RD, Snell KIE, Ensor J, et al. Minimum sample size for developing a multivariable prediction  
50 model: PART II - binary and time-to-event outcomes. *Statistics in Medicine* 2019;38(7):1276-  
51 96. doi: <https://doi.org/10.1002/sim.7992>

- 1 47. Morozov SP, Andreychenko AE, Blokhin IA, et al. MosMedData: Data set of 1110 chest CT scans  
2 performed during the COVID-19 epidemic. *DD* 2020;1(1):49-59. doi: 10.17816/dd46826  
3 [published Online First: 2020-12-30]
- 4 48. Zhang K, Liu X, Shen J, et al. Clinically applicable AI system for accurate diagnosis, quantitative  
5 measurements, and prognosis of COVID-19 pneumonia using computed tomography. *Cell*  
6 2020;181(6):1423-33.e11. doi: 10.1016/j.cell.2020.04.045
- 7 49. Goodfellow IJ, Shlens J, Szegedy C. Explaining and harnessing adversarial examples. *arXiv preprint*  
8 *arXiv:14126572* 2014
- 9 50. Snell KIE, Archer L, Ensor J, et al. External validation of clinical prediction models: simulation-  
10 based sample size calculations were more reliable than rules-of-thumb. *Journal of Clinical*  
11 *Epidemiology* 2021;135:79-89. doi: 10.1016/j.jclinepi.2021.02.011
- 12 51. Sounderajah V, Ashrafian H, Rose S, et al. A quality assessment tool for artificial intelligence-  
13 centered diagnostic test accuracy studies: QUADAS-AI. *Nature Medicine* 2021;27(10):1663-  
14 65. doi: 10.1038/s41591-021-01517-0
- 15 52. Collins GS, Dhiman P, Andaur Navarro CL, et al. Protocol for development of a reporting guideline  
16 (TRIPOD-AI) and risk of bias tool (PROBAST-AI) for diagnostic and prognostic prediction  
17 model studies based on artificial intelligence. *BMJ Open* 2021;11(7):e048008. doi:  
18 10.1136/bmjopen-2020-048008
- 19